Figure 5.1

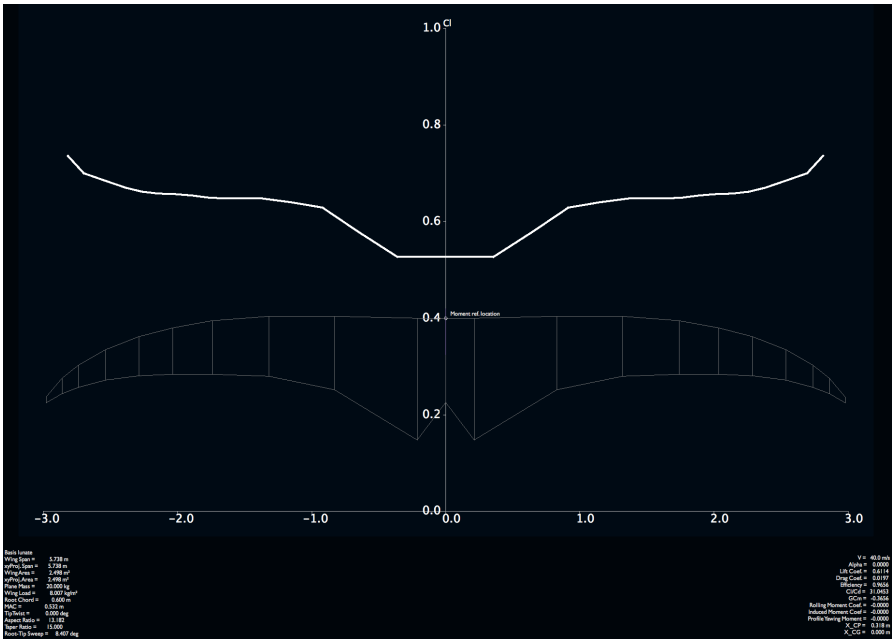

XFLR5 output showing typical spanwise variation of lift coefficient. The lift distribution is obtained from the product of the lift coefficient and local wing chord.

Figure 5.2

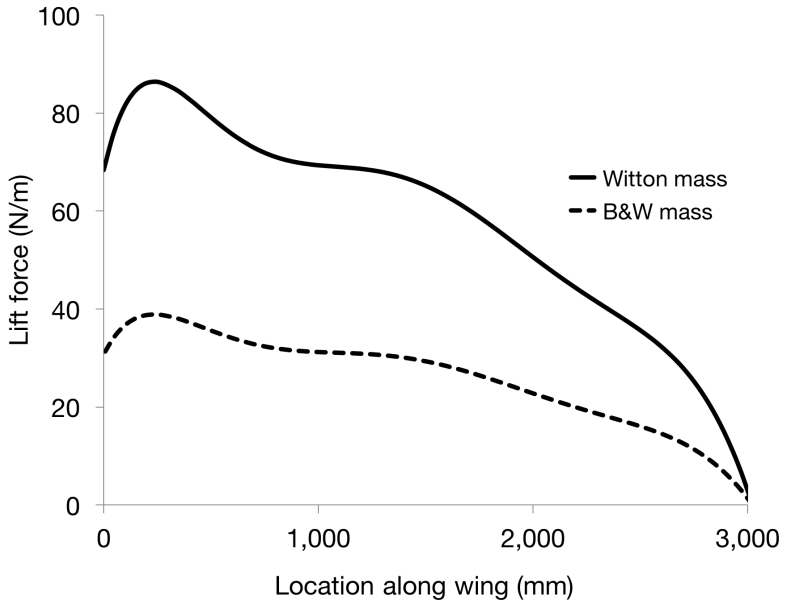

Spanwise lift distribution (N/m) for two different body mass assumptions (Witton 2008 solid line and and Bramwell & Whitfield 1974 dashed line).

Figure 5.3

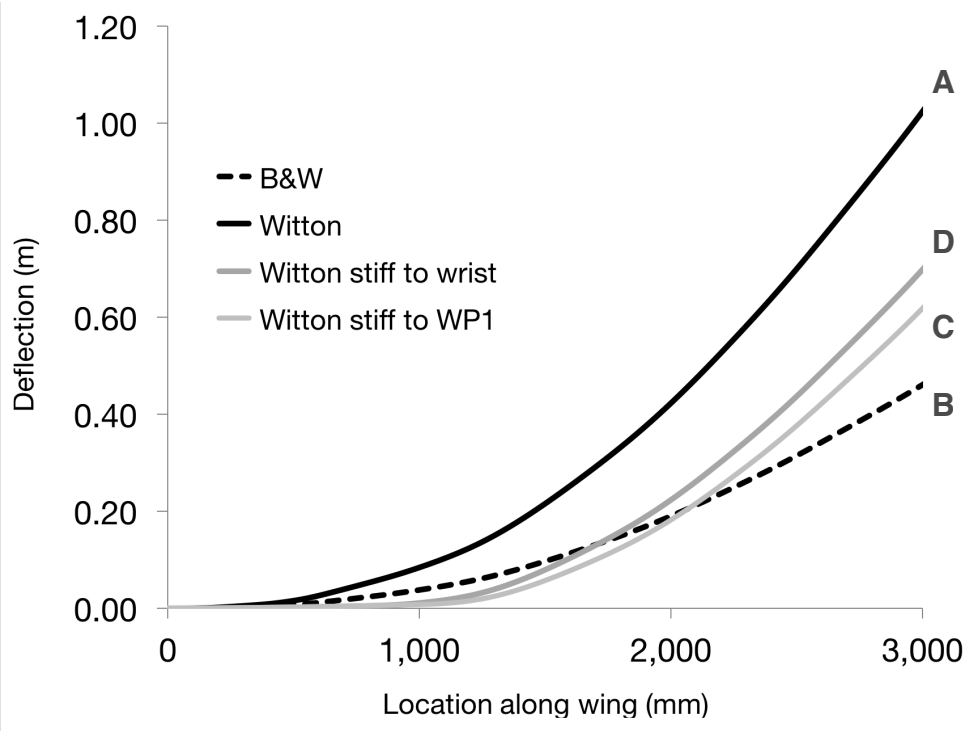

Calculated wing spar defection under different assumptions of fixity and body mass. Dark lines (A) and (B) assume spar fixed at glenoid and show effects of different mass assumptions. Grey lines for Witton (2008) mass only, but showing effect of different fixity assumptions.

Figure 5.4

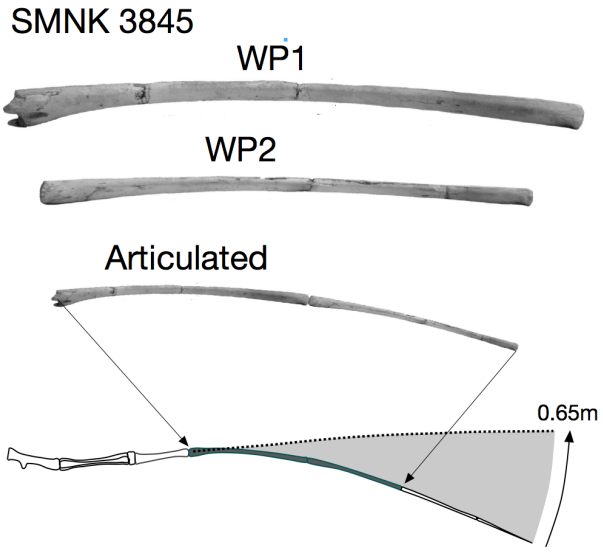

Wing reconstruction using 3D preserved wing bones from the Karlsruhe collection, which have dorsoventral curvature. The natural curvature of the wing phalanges almost equals the deflection under load, resulting in only a small tip elevation above the glenoid. (Deflection assumes Witton (2008) mass with high proximal stiffness.)

Figure 5.5

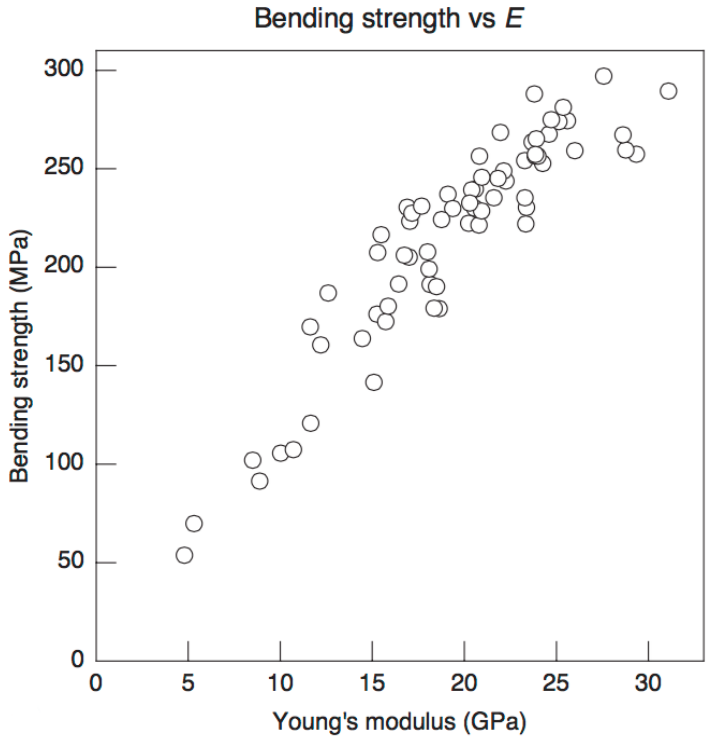

Variation of bone bending strength with Young's modulus (from Currey 2004).

Figure 5.6

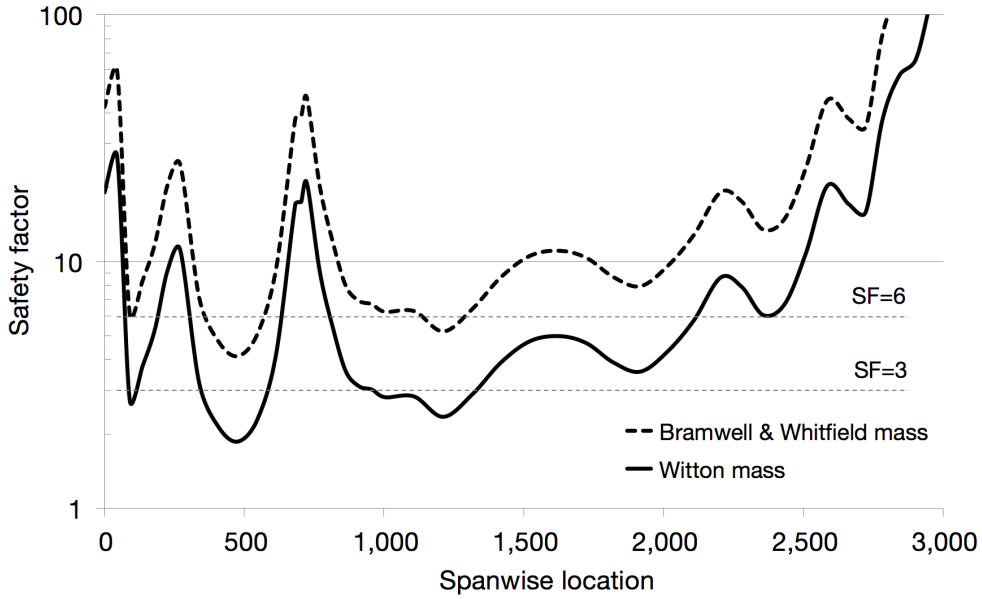

Spanwise variation of tensile stress safety factors, showing effect of different mass assumptions (sources as above.) Typically the safety factor for birds under similar loading assumptions is between 4 and 6, so the pterosaur wing spar appears relatively highly loaded.

Figure 5.7

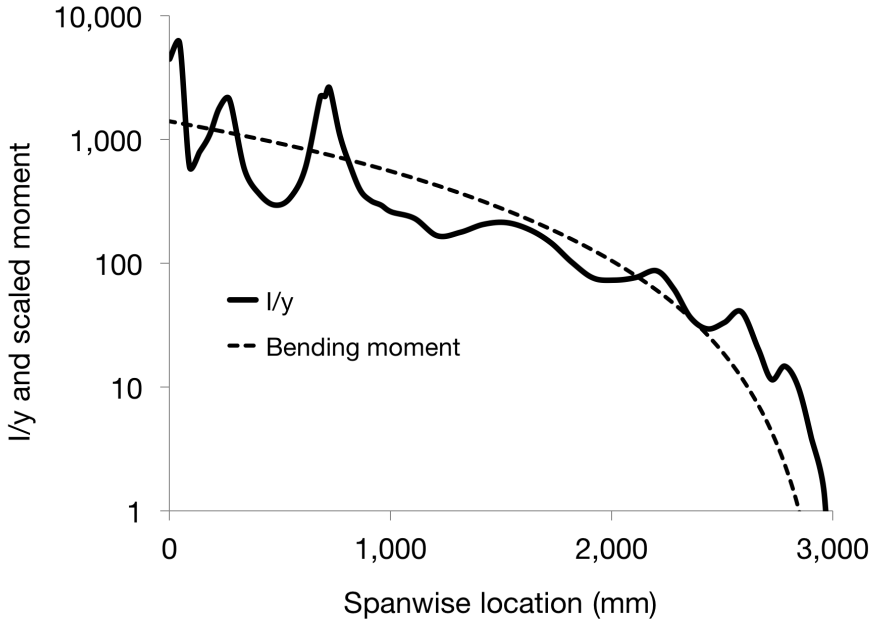

Spanwise variation of section modulus (mm^3) and bending moment arbitrarily scaled to the same axes. The curves have very similar shapes, suggesting a structure optimised to support the applied loading.